Part IV

Optical Synthesis Imaging

Chapter 12

Interferometry with Two Telescopes

H. Melvin Dyck

U.S. Naval Observatory
Flagstaff, Arizona

12.1 Introduction

As was discussed by Boden in Chapter 2, faithfully reconstructing complex astronomical images requires the use of many interferometric baselines and closure phases. Owing to phase smearing in the atmosphere, fewer than three telescopes are not capable of recovering phase information in a general way (cf. Chapter 13). However, two telescopes can recover the amplitude of the complex visibility function (Born and Wolf, 1999) and are useful for investigating a limited range of scientific problems. These problems belong to a class for which the structure is known *a priori* and only a few global parameters need to be determined from observations. As we increase the number of parameters to be extracted from models fitted to the observed visibility amplitude, we also increase the risk of misinterpreting the nature of the source. In this chapter, we concentrate on the more limited class of sources where one or two global parameters suffice to yield interesting astrophysical information. We shall also try to stress limitations to the interpretation that may arise from expected astrophysical violations to the *a priori* knowledge of the source.

12.2 Simple Concepts of Aperture Synthesis

A single-mirror telescope is able to construct accurate images because it provides a continuum of interferometric baselines ranging in size from zero up to the diameter of the mirror. The resolution of such an instrument, called the point-spread function (Schroeder,

2000), may be determined by diffraction or by aberrations either intrinsic to the mirror or introduced by an unstable atmosphere. Let's consider this in more detail. In Figure 12.1(a), we show a solid circle meant to represent the edge of a mirror of arbitrary diameter D. We refer to this part of Figure 12.1 as the "aperture plane." Let's suppose that the mirror is placed on the ground with directions to north and east as shown. If we consider any two infinitesimal sub-apertures in the mirror, represented by the small gray dots in the figure, then we may envision a single baseline, B, between them. We know from the theory of interferometry (see Chapter 2) that we may sample an image with a resolution of approximately λ/B (Schroeder, 2000) where λ is the wavelength of the observation. Inspection of the figure shows us that the we may resolve all angular scales $\theta \geq \lambda/D$ for all possible pairs of elementary sub-apertures in the mirror. This is the fundamental principle of aperture synthesis. We have synthesized the full aperture D by taking all possible pairs of elementary sub-apertures in the mirror. In this case we are dealing with a filled aperture system.
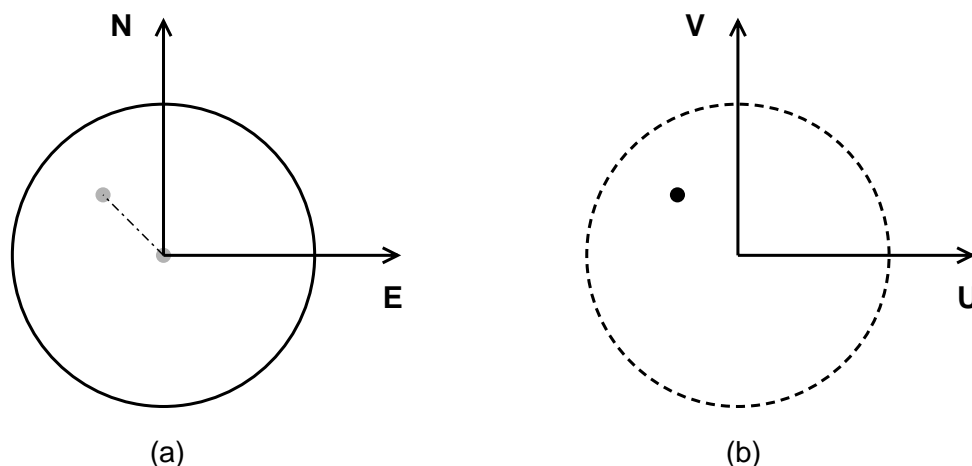
Figure 12.1: The relationship between baseline in the aperture plane and spatial frequency in the Fourier plane.

There is another plane of interest in imaging, namely the Fourier plane or (u, v) plane, shown in Figure 12.1(b). The coordinate compliment to spatial resolution in the aperture plane (λ/B) is spatial frequency, B/λ, in the Fourier plane. Note that a single baseline in the aperture plane maps into a single point in the Fourier plane. All possible baselines filling the aperture plane will map into all possible points in the Fourier plane. The filled aperture system will completely sample the Fourier plane from zero spatial frequency out to a maximum spatial frequency D/λ, equal to the radius of the dashed circle in the figure. The Fourier coordinate axes (u, v) correspond to the spatial axes E,N in the aperture plane. Note that the Fourier representation of the point-spread function is the optical transfer function while its modulus is the modulation transfer function (Schroeder, 2000).

Now suppose the solid circle in the figure is composed of a few discrete, separated sub-apertures of finite size. This is an example of an unfilled or sparse aperture system. We
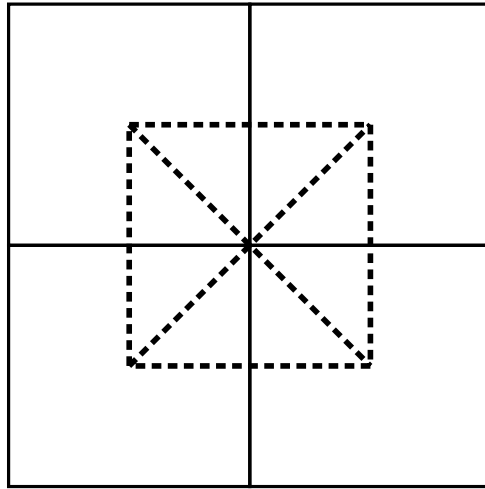
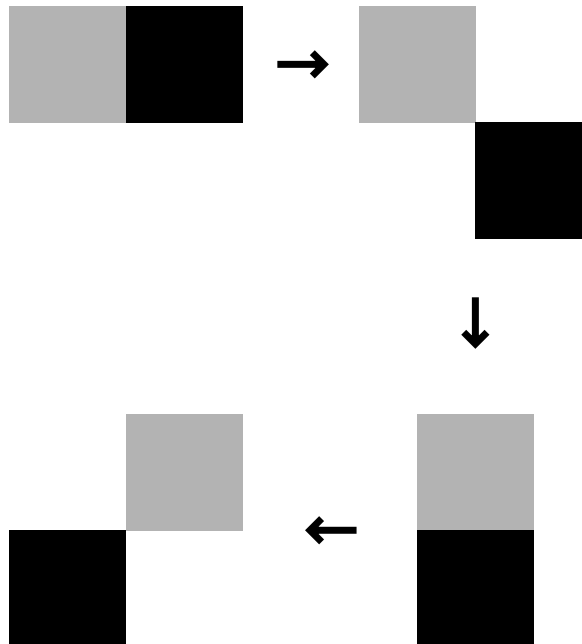Figure 12.2: All possible baselines for a 2 × 2 telescope array.

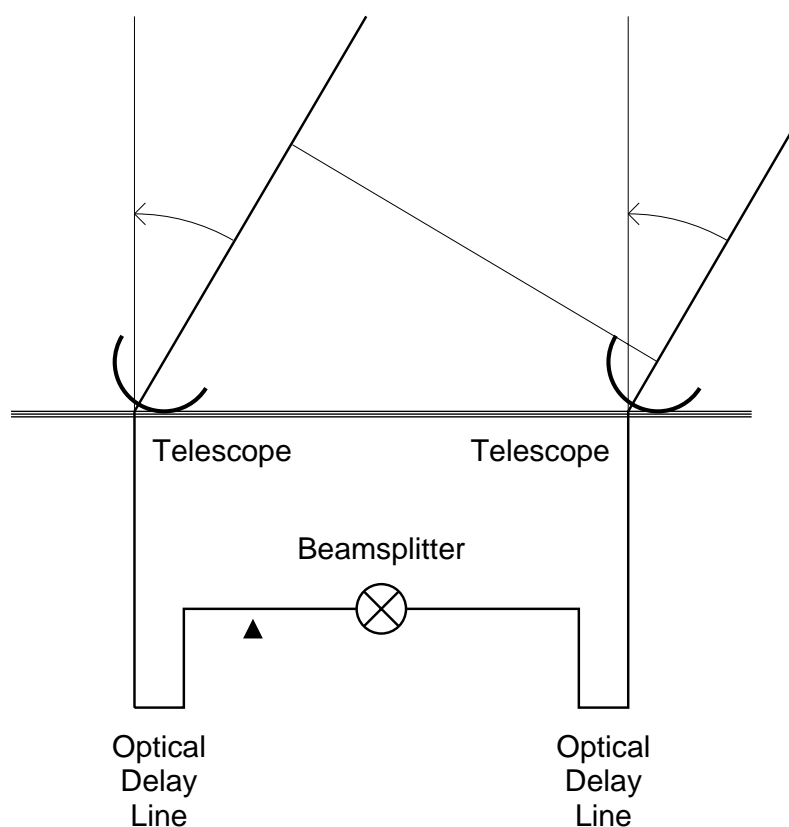Figure 12.3: Synthesizing a 2 × 2 telescope by re-positioning 2 elements.

Figure 12.4: A simple schematic picture of a two-telescope interferometer, showing the optical delay lines. With the delay lines balanced, as shown in the figure, the position of the fringe occurs at the filled triangle for the source observed to the right of the zenith.

may draw baselines between all possible pairs. For a snapshot observation (i.e. infinitesimal observation time compared to the rotation of the Earth), there will be a finite number of baselines in the aperture plane, corresponding to a finite number of spatial frequencies in the Fourier plane. As an example, we have shown in Figure 12.2 an interferometer formed from four contiguous square apertures, arranged in a 2 × 2 array. The array is shown as the solid squares in the figure. Also shown as dashed lines are the six possible baselines obtainable from the array. The point-spread and modulation-transfer functions for this array will have only discrete values. Such sparse aperture functions contribute to the difficulty of interpretation of complex images. Note also that of the six baselines shown in Figure 12.2, two are redundant, giving the same image information. The redundant pairs are the horizontal and vertical pairs in the figure.

We may synthesize the 2 × 2 interferometric array from only a single pair of telescopes, moving one or both telescopes to achieve all possible baselines. This concept is shown in Figure 12.3 in a sequence of four different configurations. So, we have illustrated how we may synthesize a larger aperture from a number of sub-apertures by physically moving the

sub-apertures. These concepts apply to the snapshot mode of observation. Of course the actual resolution of any interferometric pair is not the physical separation between the pairs but the projected separation of the pair as viewed from the source. This is illustrated in Figure 12.4, where we show the basic elements of a two-telescope interferometer including the optical delay lines and the optical correlator (labeled the beam splitter) where the interference occurs. In this figure the source is supposed to be to the right of the direction to the zenith. In order to obtain interference at the beam splitter the optical delay line for the telescope on the right would need to be adjusted to add in a path length equal to the extra distance traveled by the light rays coming to the telescope on the left. As the Earth rotates, the amount of delay changes from a maximum at the horizon to zero at the zenith.

The spatial resolution on the source is the projected distance between the two apertures as seen from the source. Clearly, this resolution will change as the telescopes track the source, ranging from zero when the source is on the horizon to some maximum value (equal to the physical separation in the figure) when the source is at the zenith. Thus, we may also synthesize an aperture by allowing the Earth to rotate for a fixed physical configuration of the array. This has been referred to as Earth rotation aperture synthesis.

12.3   Optical Delay and (u, v) Plane Tracks

For any given array the aperture synthesis process involves a combination of physical movement of the telescopes in the array and Earth's rotation. An interferometer with many telescopes will sweep out much of the (u, v) plane corresponding to all the possible baselines. A two-telescope interferometer has much sparser coverage in the (u, v) plane. A nice discussion of the equations for the u and v coordinates for a pair of telescopes is developed in the paper by Fomalont and Wright (1974), for example. We follow their formalism in this chapter. In Figure 12.5 we sketch out the coordinate frame for the development. Let the origin of the coordinate system be centered on one of the mirrors of the pair. One axis points north, one points east, and one points to the zenith; these axes are shown as solid lines and are labeled N, E, and L in the figure. We may draw a vector **B**, shown as a dashed line in the figure, from one mirror to the other that has components B_E, B_N, and B_L. Let b = mean latitude of the interferometer (and neglecting curvature of the Earth), δ = declination of the source, and h = hour angle of the source. The (u, v) coordinates corresponding to a snapshot projection of the baseline, in spatial frequency units (cycles/arcsec), are

$$u \; = \; (\, B_E \cos h - B_N \sin b \sin h + B_L \cos b \sin h \,) \,/\, 206265\,\lambda, \qquad (12.1)$$

and

$$v \; = (\, B_E \sin \delta \sin h \quad + \quad B_N(\sin b \sin \delta \cos h + \cos b \cos \delta)$$
$$- \quad B_L(\cos b \sin \delta \cos h - \sin b \cos \delta) \;) \; / 206265\,\lambda.$$

We have computed the (u, v) plane tracks for a simple two-telescope interferometer situated at a latitude $b = 33°$, having baseline components $B_E = B_N = 100$ m and operated at

$\lambda = 2.2$ μm. Tracks are shown for sources at four different declinations assuming the interferometer tracks the source over the range of hour angles $-4 \leq h \leq +4$. These tracks are shown plotted in Figure 12.6 which illustrates how little of the (u, v) plane is filled by this simple interferometer. One could laboriously move the telescopes and repeat the observations but this is not so important for the simple sources we will consider in this chapter. We may also see the dependence of the tracks upon source position. Note that not only does the projected separation change but also the orientation of the baseline with respect to the source changes as the Earth rotates.

To finish this section we give below the relation for the optical delay (in the same units as the baseline vector components) in terms of telescope and source parameters.

$$
\begin{align}
\Delta \; = \; & - \; B_E \, \cos\delta \, \sin h \tag{12.2} \\
& - \; B_N \, (\sin b \, \cos\delta \, \cos h - \cos b \, \sin\delta) \tag{12.3} \\
& + \; B_L \, (\cos b \, \cos\delta \, \cos h + \sin b \, \sin\delta). \tag{12.4}
\end{align}
$$

12.4   Simple Models of Astrophysical Sources

In this section we apply the principles discussed in the previous section but limit them to a two-telescope interferometer. A simplification adopted for the models is that the visibilities are observed along a single, arbitrary, radial cut through the source. For this case we will plot visibility amplitude $V(s)$ as a function of spatial frequency s.

One may think of several astrophysical systems where observations at a few baseline separations and azimuths, projected on the source, will serve to characterize the system. Some of these simple systems and the relevant astrophysical parameters are listed below:

- Binary stars (one may obtain stellar masses)

- Single-star angular diameters (one may obtain linear radii and effective temperatures)

- Limb-darkened diameters (one may obtain the atmospheric temperature structure)

- Circumstellar shells (one may characterize mass-loss phenomena)

- Departures from circular symmetry in stars (one may detect non-radial pulsation and rapid rotation).

Of course, it is understood that other pieces of information are needed to derive the parameters mentioned above. All of the above systems present relatively simple visibility curves that may be adequately sampled by a two-telescope interferometer.
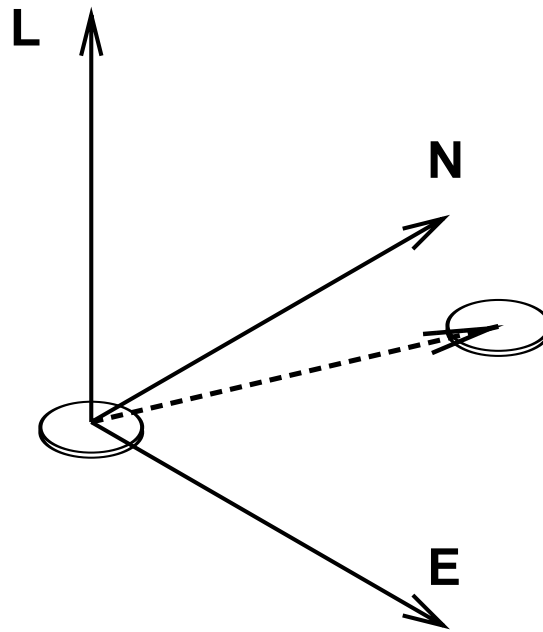
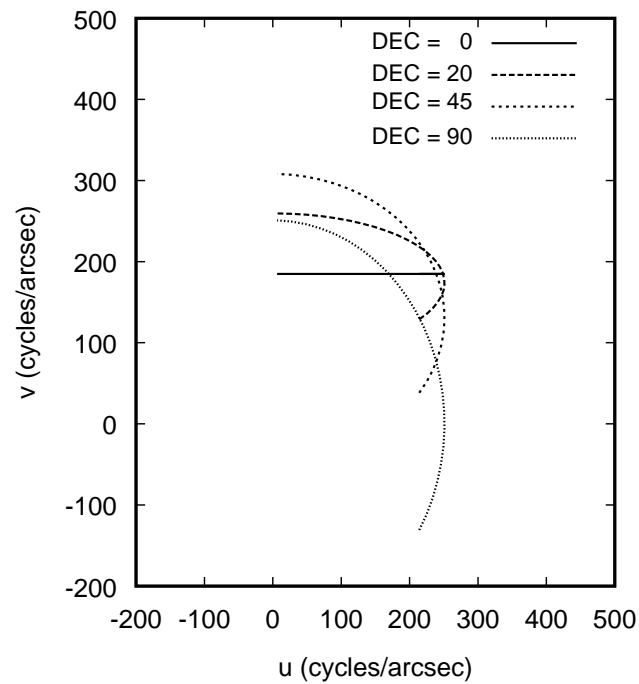Figure 12.5: The three-axis coordinate system for a two-telescope interferometer.

Figure 12.6: (u, v) tracks for a two-telescope interferometer for sources at different declinations and observed over a range of hour angles 4 hours either side of the meridian.
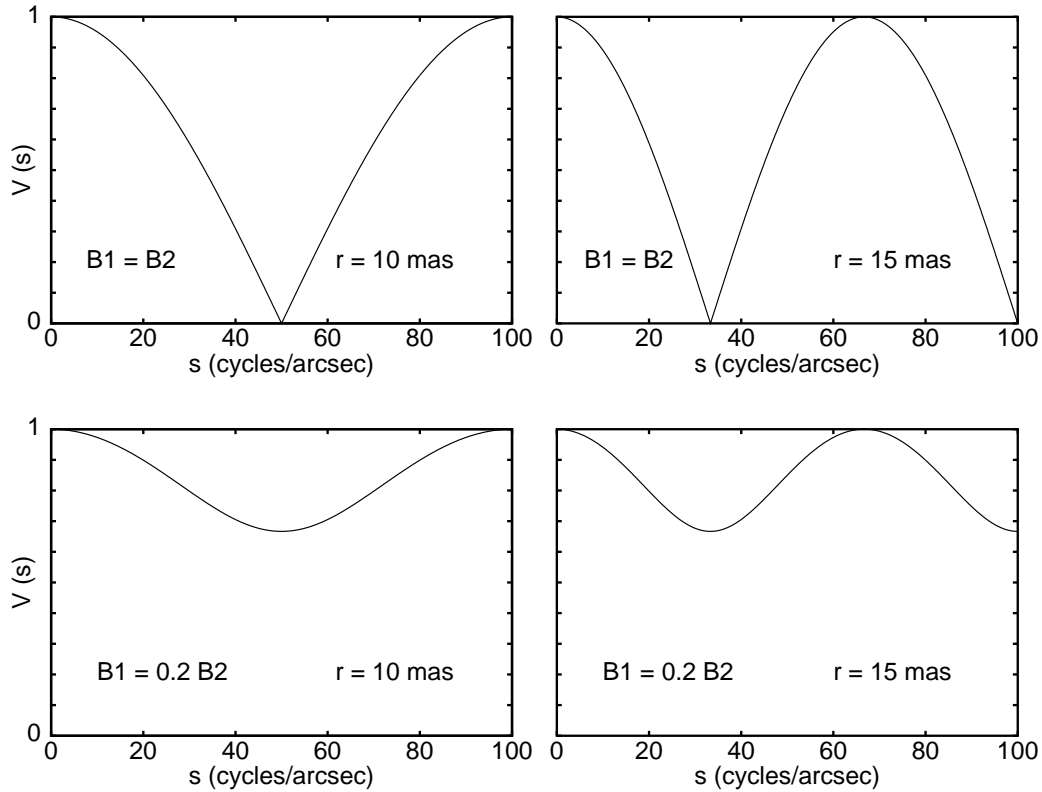
Figure 12.7: Double-star visibility curves. Note how the position and depth of the minima change with separation and brightness ratio, respectively.

12.4.1   Binary Stars

Let's begin with a binary star system. We suppose that both stars are unresolved and define B_1 = brightness of source 1, B_2 = brightness of source 2 and r = separation between sources (measured in arcsec). The visibility amplitude may be shown to be

$$V(s) = \left[P_0 + (1 - P_0)\cos^2(\pi s r)\right]^{1/2}, \tag{12.5}$$

where the parameter P_0 is defined as

$$P_0 = \left(\frac{B_1 - B_2}{B_1 + B_2}\right)^2. \tag{12.6}$$

In Figure 12.7 we have plotted some examples of two unresolved points, where we have varied the spacing and brightness ratio for the two components. One may see that the closer together the stars become, the more cycles occur in the visibility amplitude function. Also, when the stars are equally bright, the first minimum of the visibility amplitude goes to zero. Note that the first minimum becomes shallower as the brightness ratio changes

from unity. The properties of the first minimum may be used to determine the separation and brightness ratio for the stars. If we let $V_{\min}$ = amplitude of the first minimum in the visibility function and $s_{\min}$ = spatial frequency corresponding to that first minimum then we find that

$$r = \frac{1}{2s_{\min}},$$ (12.7)

and

$$\frac{B_1}{B_2} = \frac{1 + V_{\min}}{1 - V_{\min}}.$$ (12.8)

Note that the separation obtained in this way will be the component of the binary separation in one direction, the direction given by the interferometer baseline. To determine the true separation, this measurement must be repeated in at least one other direction. Normally, by observing a binary system for an extended period during the night, one would obtain snapshot values of $V(s)$ for a variety of projected telescope separations and orientations with respect to the source. These observations may be used to solve for the binary source parameters. Obvious possible problems with such observations would arise if the source had additional components or if one or both stars were resolved.

Fruitful binary star investigations have been carried out at the Mark III (Hummel *et al.*, 1995), IOTA (Dyck *et al.*, 1995), PTI (Boden *et al.*, 1999) and NPOI (Hummel *et al.*, 1998) among others.

12.4.2 Stellar Angular Diameters

Next we consider single-star angular diameters and suppose that the stars appear as simple, circular, uniformly-bright disks projected on the sky. If a = diameter of the source (in arcsec) then the visibility function may be shown to be

$$V(s) = \left| \frac{2J_1(\pi a s)}{\pi a s} \right|,$$ (12.9)

where $J_1(\pi a s)$ is the first-order Bessel function of the first kind. In Figure 12.8 we have plotted visibility functions for sources of three different diameters. Note that successive secondary maxima decrease in amplitude with increasing spatial frequency. The frequency of the first zero of the function, s_0, scales inversely with the angular diameter of the source such that $a \simeq 1.22/s_0$. In principle, if we know that the source really is a uniformly-bright circular disk, the angular diameter may be determined from the measurement of the visibility amplitude at a single spatial frequency. For example, when $V(s) \geq 0.13$, approximately, then we know that the measurement lies at spatial frequencies smaller than s_0. A single measurement may be used to obtain the diameter uniquely.

Interferometric investigations of single star diameters have been carried out by Michelson and Pease (1921), Di Benedetto and Rabbia (1987), Mozurkewich *et al.* (1991), Dyck *et al.* (1998), van Belle *et al.* (1999), and Nordgren *et al.* (1999).

Obvious difficulties with the interpretation will arise if there are spots on the surface or in the presence of limb-darkening. Surface structure, in general, will be too complex to be treated adequately by observations with two telescopes. Limb darkening may be assumed to be circularly symmetric and primarily affects the part of the visibility curve at frequencies $s \geq s_0$, where it depresses the visibility curve below the value derived from uniformly-bright circular disks. At the present time model atmosphere calculations exist that allow one to estimate more realistic center-to-limb brightness variations than can be obtained from the assumption of a uniformly bright circular disk. One should consult, for example, recent work by Claret (1998) for stars hotter than about 4000 K and Hofmann and Scholz (1998) for cooler, more extended stars. These papers will lead the reader to other investigations. A convenient analytic expression for the center to limb brightness variations was developed by Michelson and Pease (1921) and suggested by Hestroffer (1997) as a useful approximation to the models. In image space this has the form

$$\frac{I(\mu)}{I(0)} = \mu^{\alpha}, \tag{12.10}$$

where $I(\mu) = $ disk brightness at angle μ, $\mu = \cos\theta$, and $\alpha = $ an exponent best describing the model atmosphere. The angle θ is the angle between the normal to the stellar surface and the direction to the observer, at the point observed on the star. Hestroffer (1997) has obtained an analytic form for the visibility from this center to limb brightness function:

$$V(s) = \Gamma(n+1) \frac{|J_n(\pi a s)|}{(\pi a s/2)^n}, \tag{12.11}$$

where $n = (\alpha + 2)/2$.

Direct determination of limb darkening has been carried out by Hajian *et al.* (1998).

12.4.3   Circumstellar Shells

Circumstellar shell structures may be detected if they are optically thin, for example, as superpositions on the underlying star. Suppose we modeled such a system by a coaxial uniform disk and point source. Here, the uniform disk represents the shell while the point source represents the central star. Let $a = $ diameter of the shell and $V_P = $ ratio of power radiated by the star to total power radiated by the system. The visibility function for this combination may be shown to be

$$V(s) = V_P + (1 - V_P) \left[\frac{2\, J_1(\pi a s)}{\pi a s} \right]. \tag{12.12}$$

An example of this kind of visibility function has been shown in Figure 12.9.

Observations of circumstellar shells superposed on central stars have been made with the ISI interferometer. Reports of these observations may be found, for example, in Danchi *et al.* (1994). One may see examples of composite visibility functions such as the one described above in this paper.
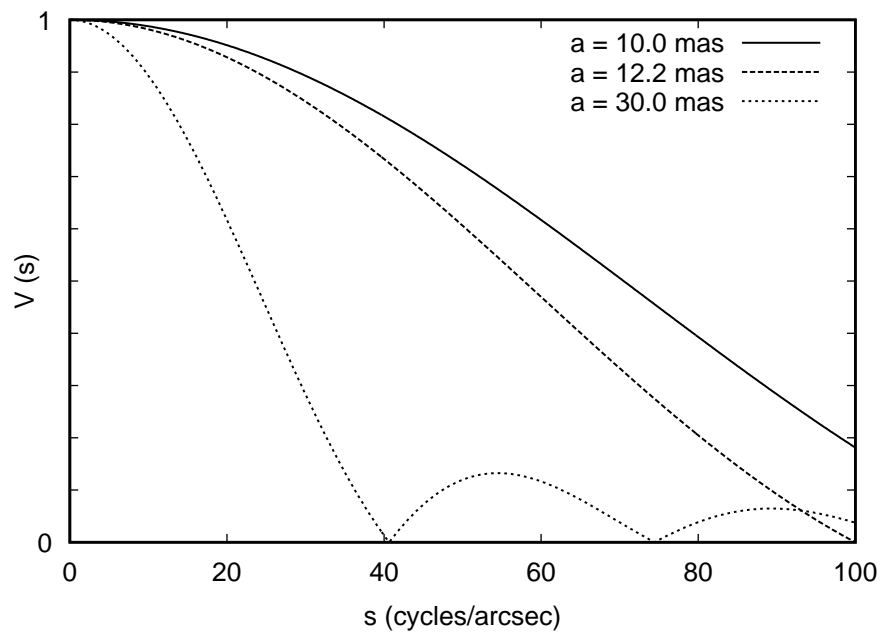
Figure 12.8: Visibility curves for uniformly-bright circular disks. Note the decreasing amplitude of successive maxima beyond the first null.
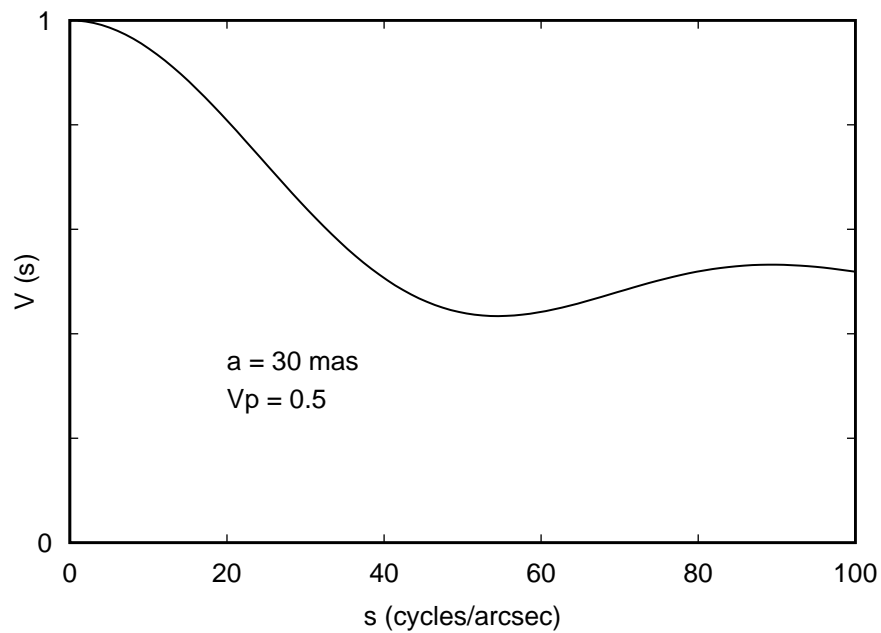

Figure 12.9: The visibility curve for a uniform-disk surrounding a point. The disk size is 30 mas and there is 50% in each of the two components.

We finish this section with a brief mention of departures from circular symmetry. For simple stars, one may detect this departure by observing at more than one angle projected on the star. Fitting a uniform disk or limb darkened disk visibility function to the observations will show a different scale size in different directions.

12.5   Cautions and Caveats

The most important limitation imposed upon the choice of model is set by the resolution. It is stating the obvious that very poor angular resolution may render a source unresolved. As the resolution is improved there will be a regime where the source is seen to be different from a point but for which there will be nearly complete uncertainty about its nature. It is an interesting exercise to take the model formulations presented in the previous section, choose variable size scales for each model and see how closely the visibilities can be made to agree at the very lowest spatial frequencies.

Apart from these sampling considerations, the choice of model for any set of observations will depend upon the signal-to-noise ratio of the observations, the confidence in the level of systematic errors in the system, the number and orientation of the baselines used and the expected complexity of the source brightness distribution.

12.6   Comparisons

There are now enough interferometers operating that we may reasonably ask about the quality of the measurements. There are two easy ways to do this, in the absence of ground truth observations. First, one may inter-compare interferometers measuring the same objects. Second, one may compare the measurements of interferometers with the most current predictions of models. Neither of these methods defines the absolute accuracy of interferometric observations.

Let's first compare measurements of the same objects made with different interferometers. In Figure 12.10 the fractional difference between 2.2 μm measurements made at IOTA (Dyck *et al.*, 1998) and those made at CERGA (Di Benedetto and Rabbia, 1987) or FLUOR (Perrin 1996; Perrin *et al.* 1998a,b) is plotted versus the IOTA diameter. Here, diameters obtained from uniform disk fits to the visibility data are used, with no corrections made for the effects of limb darkening. The important points of the figure are that (1) there is no large systematic difference among the measurements and (2) the scatter is larger for the smaller diameter stars. Quantitatively, the mean systematic difference between the IOTA measurements and the other measurements is (Other IR $-$ IOTA)/IOTA $= 0.017 \pm 0.107$ (rms). That is, the IOTA uniform disk diameters are less than 2% smaller than the other diameters, with a typical error of about 11% for a single measurement. Most of the error in the measurements is attributable to the measurement error of the IOTA diameters.
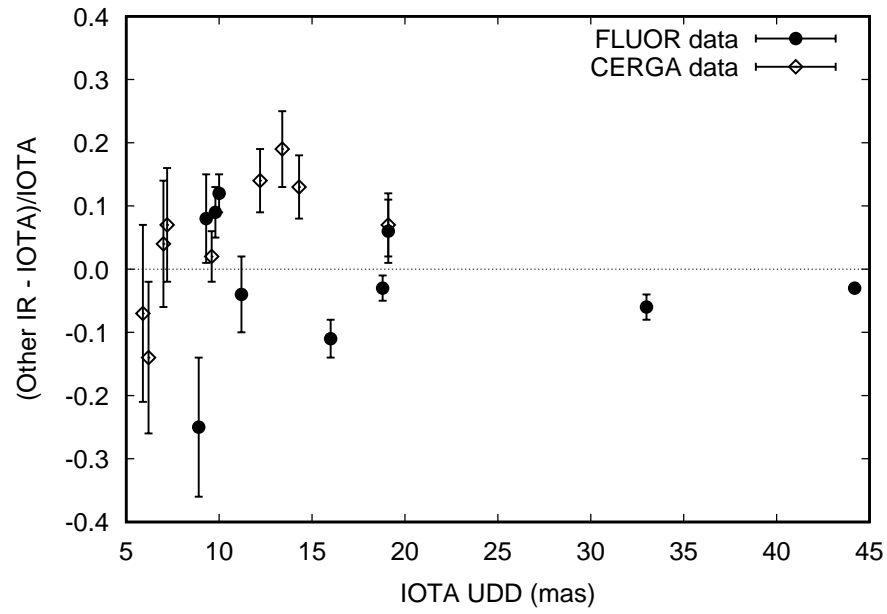
Figure 12.10: A comparison of 2.2-μm uniform disk diameters measured with IOTA to those measured with CERGA and FLUOR.
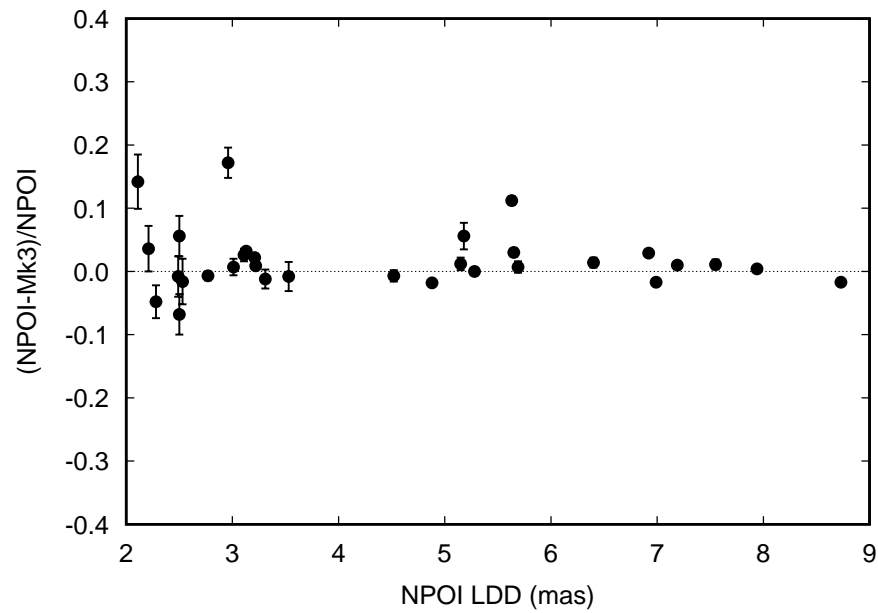

Figure 12.11: A comparison of limb-darkened angular diameters measured at NPOI and the Mark III at red wavelengths.

In Figure 12.11, the same comparison is made between the NPOI and the Mark III for stars measured in common at wavelengths near 800 nm. These results have been tabulated by Nordgren (1999). Here, the comparison is between limb-darkened angular diameters, since the observations at the two interferometers were made at somewhat different wavelengths. Note again the relative increase in scatter for the smaller diameter stars. The quantitative systematic difference is (NPOI − Mark III)/NPOI = 0.018 ± 0.052. That is, the NPOI diameters are less than 2% larger than the Mark III diameters with a typical error of the diameter of about 5%.

Thus, optical and infrared interferometers working at the same or nearly the same wavelengths are capable of reproducing each others results to levels better than about 2%.

Next, we may compare interferometric observations to current model predictions. Blackwell *et al.* (1990) and Blackwell and Lynas-Gray (1994), using the infrared flux method (IRFM), have computed and tabulated diameters for stars in the temperature range 4000–8500 K. Bell and Gustafsson (1989) have also tabulated diameters, but that are not based principally upon infrared observations. The largest overlap between observed and computed diameters exists for the near infrared, so we have used the 2.2-μm observations made at IOTA by Dyck *et al.* (1998), at CERGA by Di Benedetto and Rabbia (1987) and at PTI by van Belle *et al.* (1999). These comparisons are shown plotted in Figure 12.12, where IRFM refers to the diameters from Blackwell and collaborators and BG refers to the diameters from Bell and Gustafsson. In this figure, the comparison is made between the fractional difference in diameter and the intrinsic V−K color of the star. One may see that the general level of the difference is less than about 20% with the exception of 41 Cyg, the very discrepant point in the upper left part of the figure. Excluding this star, the comparisons are (Observed − IRFM)/IRFM = -0.019 ± 0.061 and (Observed − BG)/BG = -0.009 ± 0.071. That is, the observations and the models agree to the level 1–2%. If the 41 Cyg diameter is left in the plot, there is a suggestion that there may be a difference between theory and observation that depends upon color. This will have to be verified with additional observations.

A final assessment of the capability of interferometers may be obtained from double star observations. In Figure 12.13 there is a plot of the orbital position of the secondary about the primary for Mizar A, taken from Hummel *et al.* (1998). Data are shown from both the Mark III and the NPOI at optical wavelengths. The best fit orbit yields an (observed − computed)$_{rms} \simeq 60$ μas!
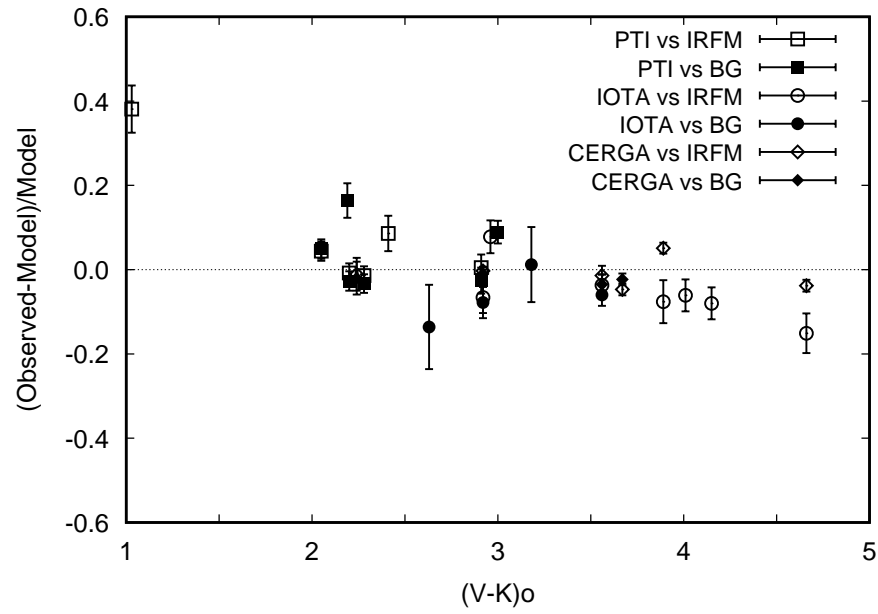
Figure 12.12: A comparison of angular diameters computed from model stellar atmospheres and limb-darkened diameters obtained at 2.2 μm. The codes are explained in the text.
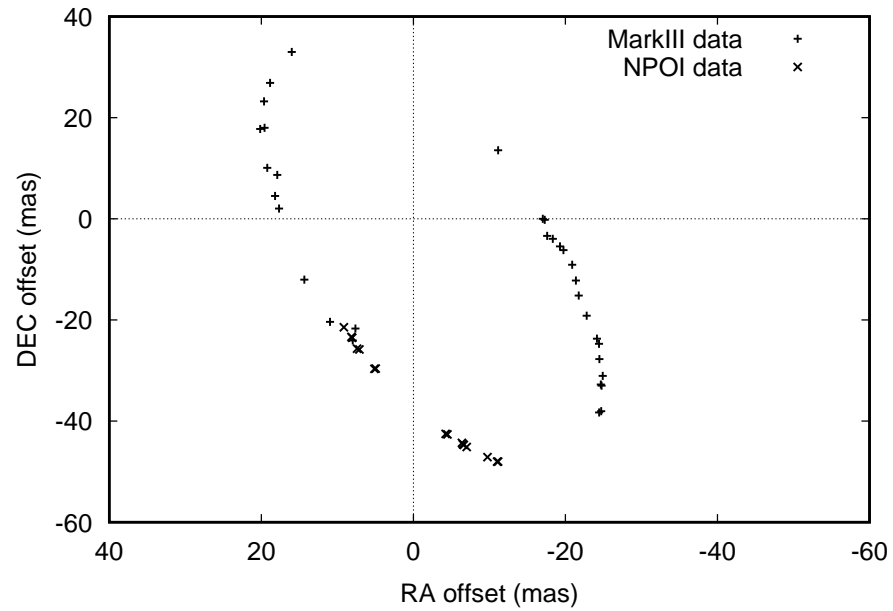

Figure 12.13: Observations of the apparent orbit for the binary star Mizar A.

References

R.A. Bell and B. Gustafsson, "The effective temperatures and colours of G and K stars," Mon. Not. R. Astron. Soc. **236**, 653–708 (1989).

G.T. van Belle, B.F. Lane, R.R. Thompson, A.F. Boden, M.M. Colavita, P.J. Dumont, D.W. Mobley, D. Palmer, M. Shao, G.X. Vasisht, J.K. Wallace, M.J. Creech-Eakman, C.D. Koresko, S.R. Kulkarni, X.P. Pan, and J. Gubler, "Radii and effective temperatures for G, K, and M giants and supergiants," Astron. J. **117**, 521–533 (1999).

G.P. Di Benedetto and Y. Rabbia, "Accurate angular diameters and effective temperatures for eleven giants cooler than K0 by Michelson interferometry," Astron. Astrophys. **188**, 114–124 (1987).

D.E. Blackwell and A.E. Lynas-Gray, "Stellar effective temperatures and angular diameters determined by the infrared flux method (IRFM): revisions using improved Kurucz LTE atmospheres," Astron. Astrophys. **282**, 899–910 (1994).

D.E. Blackwell, A.D. Petford, S. Arribas, D.J. Haddock, and M.J. Selby, "Determination of temperatures and angular diameters of 114 F-M stars using the infrared flux method (IRFM)," Astron. Astrophys. **232**, 396–410 (1990).

A.F. Boden, C.D. Koresko, G.T. van Belle, M.M. Colavita, P.J. Dumont, J. Gubler, S.R. Kulkarni, B.F. Lane, D. Mobley, M. Shao, J.K. Wallace, and G.W. Henry, "The visual orbit of ι Pegasi," Astrophys. J. **515**, 356–364 (1999).

M. Born and E. Wolf, *Principles of Optics*, 7 (expanded) edn. (Cambridge, UK: Cambridge University Press, 1999).

A. Claret, "Comprehensive tables for the interpretation and modeling of the light curves of eclipsing binaries," Astron. Astrophys. Supp. Ser. **131**, 395–400 (1998).

W.C. Danchi, M. Bester, C.G. Degiacomi, L.J. Greenhill, and C.H. Townes, "Characteristics of dust shells around 13 late-type stars," Astron. J. **107**, 1469–1513 (1994).

H.M. Dyck, G.T. van Belle, and R.R. Thompson, "Radii and effective temperatures for K and M giants and supergiants. II," Astron. J. **116**, 981–986 (1998).

H.M. Dyck, J.A. Benson, and F.P. Schloerb, "Imaging a binary star with a two-telescope Michelson interferometer," Astron. J. **110**, 1433–1439 (1995).

E.B. Fomalont and M.C.H. Wright, "Interferometry and aperture synthesis," in *Galactic and Extra-galactic Radio Astronomy*, G.L. Verschuur and K.I. Kellerman, eds., 256–290 (New York: Springer-Verlag, 1974).

A.R. Hajian, J.T. Armstrong, C.A. Hummel, J.A. Benson, D. Mozurkewich, T.A. Pauls, N.M. Elias II D.J. Hutter, K.J. Johnston, L.J. Rickard, and N.M. White, "Direct confirmation of stellar limb darkening with the Navy Prototype Optical Interferometer," Astrophys. J. **496**, 484–489 (1998).

D. Hestroffer, "Centre to limb darkening of stars," Astron. Astrophys. **327**, 199–206 (1997).

K.-H. Hofmann and M. Scholz, "Limb-darkening and radii of non-Mira M giant models," Astron. Astrophys. **335**, 637–646 (1998).

C.A. Hummel, J.T. Armstrong, D.F. Buscher, D. Mozurkewich, A. Quirrenbach, and M. Vivekanand, "Orbits of small angular scale binaries resolved with the Mark III interferometer," Astron. J. **110**, 376–390 (1995).

C.A. Hummel, D. Mozurkewich, J.T. Armstrong, A.R. Hajian, N.M. Elias II, and D.J. Hutter, "Navy Prototype Optical Interferometer observations of the double stars Mizar A and Matar," Astron. J. **116**, 2536–2548 (1998).

A.A. Michelson and F.G. Pease, "Measurement of the diameter of α Orionis with the interferometer," Astrophys. J. **53**, 249–259 (1921).

D. Mozurkewich, K.J. Johnston, R.S. Simon, P.F. Bowers, R. Gaume, D.J. Hutter, M.M. Colavita, M. Shao, and X.P. Pan, "Angular diameter measurements of stars," Astron. J. **101**, 2207–2219 (1991).

T.E. Nordgren, "Stellar angular diameters from the NPOI and Mark III: A comparison," Bull. Am. Astron. Soc. **194**, 8205 (1999).

T.E. Nordgren, M.E. Germain, J.A. Benson, D. Mozurkewich, J.J. Sudol, N.M. Elias II, A.R. Hajian, N.M. White, D.J. Hutter, K.J. Johnston, F.S. Gauss, J.T. Armstrong, T.A. Pauls, and L.J. Rickard, "Stellar angular diameters of late-type giants and supergiants measured with the Navy Prototype Optical Interferometer," Astron. J. **118**, 3032–3038 (1999).

G. Perrin, *A fiber recombination unit for the IOTA interferometer: Application to the study of late-type stars*, Ph.D. thesis, Université de Paris VII (1996).

G. Perrin, V. Coudé du Foresto, S.T. Ridgway, J.-M. Mariotti, N.P. Carleton, and W.T. Traub, "Stellar parameters with high-accuracy visibilities," in *Fundamental Stellar Parameters: The Interaction Between Observation and Theory*, T. R. Bedding, A.J. Booth, and J. Davis, eds., 18–21 (Dordrecht: Kluwer Academic, 1998a).

G. Perrin, V. Coudé du Foresto, S.T. Ridgway, J.-M. Mariotti, W.A. Traub, N.P. Carleton, and M.G. Lacasse, "Extension of the effective temperature scale of giants to types later than M6," Astron. Astrophys. **331**, 619–626 (1998b).

D.J. Schroeder, *Astronomical Optics*, 2 edn. (San Diego, CA: Academic Press, 2000).